galaxies

MDPI

Article

Effelsberg Monitoring of a Sample of RadioAstron Blazars: Analysis of Intra-Day Variability

Jun Liu [1,2,3,*], **Hayley Bignall** [4] , **Thomas P. Krichbaum** [1], **Xiang Liu** [2,3], **Alex Kraus** [1],
Yuri Y. Kovalev [5,6,1] , **Kirill V. Sokolovsky** [5,7,8], **Emmanouil Angelakis** [1] **and J. Anton Zensus** [1]

[1] Max-Planck-Institut für Radioastronomie, Auf dem Hügel 69, D-53121 Bonn, Germany;
    tkrichbaum@mpifr-bonn.mpg.de (T.P.K.); akraus@mpifr-bonn.mpg.de (A.K.); yyk@asc.rssi.ru (Y.Y.K.);
    eangelakis@mpifr-bonn.mpg.de (E.A.); azensus@mpifr-bonn.mpg.de (J.A.Z.)
[2] Xinjiang Astronomical Observatory, CAS, 150 Science 1-Street, Urumqi 830011, China; liux@xao.ac.cn
[3] Key Laboratory of Radio Astronomy, Chinese Academy of Sciences, Urumqi 830011, China
[4] CSIRO Astronomy and Space Science, P.O. Box 1130, Bentley, WA 6102, Australia; hayley.bignall@csiro.au
[5] Astro Space Center of Lebedev Physical Institute, Profsoyuznaya 84/32, 117997 Moscow, Russia;
    kirx@kirx.net
[6] Moscow Institute of Physics and Technology, Dolgoprudny, Institutsky per., 9, 141700 Moscow, Russia
[7] IAASARS, National Observatory of Athens, Vas. Pavlou & I. Metaxa, 15236 Penteli, Greece
[8] Sternberg Astronomical Institute, Moscow State University, Universitetskii pr. 13, 119992 Moscow, Russia
* Correspondence: jliu@mpifr-bonn.mpg.de

check for updates

Abstract: We present the first results of an ongoing intra-day variability (IDV) flux density monitoring program of 107 blazars, which were selected from a sample of RadioAstron space very long baseline interferometry (VLBI) targets. The IDV observations were performed with the Effelsberg 100-m radio telescope at 4.8 GHz, focusing on the statistical properties of IDV in a relatively large sample of compact active galactic nuclei (AGN). We investigated the dependence of rapid ($<$3 day) variability on various source properties through a likelihood approach. We found that the IDV amplitude depends on flux density and that fainter sources vary by about a factor of 3 more than their brighter counterparts. We also found a significant difference in the variability amplitude between inverted- and flat-spectrum radio sources, with the former exhibiting stronger variations. γ-ray loud sources were found to vary by up to a factor 4 more than γ-ray quiet ones, with 4σ significance. However a galactic latitude dependence was barely observed, which suggests that it is predominantly the intrinsic properties (e.g., angular size, core-dominance) of the blazars that determine how they scintillate, rather than the directional dependence in the interstellar medium (ISM). We showed that the uncertainty in the VLBI brightness temperatures obtained from the space VLBI data of the RadioAstron satellite can be as high as ~70% due to the presence of the rapid flux density variations. Our statistical results support the view that IDV at centimeter wavelengths is predominantly caused by interstellar scintillation (ISS) of the emission from the most compact, core-dominant region in an AGN.

Keywords: galaxies; active-method; statistical-radio continuum; ISM

1. Introduction

RadioAstron is an international collaborative mission with a 10-m radio telescope onboard the SPEKTR-R spacecraft launched in July 2011 [1–3]. The space telescope observes at wavelengths of 92 cm (324 MHz, P-band), 18 cm (1.7 GHz, L-band), 6 cm (4.8 GHz, C-band), and 1.3 cm (22.2 GHz, K-band), forming space very long baseline interferometry (space VLBI, or SVLBI) together with ground-based radio telescopes, with the highest angular resolution achievable (e.g., ~7 μ as at the K-band) so far.

One of the Key Science Projects (KSPs) of the space mission is to investigate the extremely high brightness temperature of active galactic nuclei (AGNs) with the unprecedented long baselines of up to 28 Earth diameters, which will significantly improve our understanding on the mechanisms of AGN radio emissions close to the central engine. Coordinated ground-based flux density monitoring of the RadioAstron targets at centimeter wavelengths is essential to estimate the effect of interstellar scintillation (ISS) on the SVLBI visibilities. As for an ISS 'screen' within a few hundred parsecs from the Sun, the characteristic scale of scintillation pattern is comparable to the length of the RadioAstron VLBI baseline.

In order to measure the magnitudes and timescales of ISS of blazars observed by RadioAstron, in 2014 we started a RadioAstron target-triggered flux monitoring program with the Effelsberg 100-m radio telescope at 4.8 GHz. The single dish ISS monitoring and space VLBI with RadioAstron offer independent probes of the structure of blazar 'cores' at microarcsecond angular scales. Direct measurements of the sizes of scintillating sources with RadioAstron help to determine properties of the interstellar scattering screens, such as their distance and scattering strength. In turn, the focusing and defocusing effects of ISS may have a significant influence on the measured space VLBI visibilities, and it is essential to understand these effects for a complete analysis of the RadioAstron data. Thus, these two probes of microarcsecond-scale structure are highly complementary.

In the cm regime, rapid flux density variations at timescales of a day or less, known as intra-day variability (IDV, [4,5]), are frequently observed in compact flat-spectrum radio sources. IDV is present in a significant fraction (~20–50%) of flat-spectrum radio sources (e.g., quasars and BL Lac objects) [6,7]. The physical mechanism responsible for such variability remains open for debate, with models involving both source-extrinsic and -intrinsic explanations. In many cases the IDV phenomenon is explained by scattering of radio waves by turbulent ionized structures in the Milky Way (e.g., [8–13]). On the other hand, some observational evidence, such as large polarization swing, frequency dependence of IDV amplitude, multi-frequency correlation/anti-correlation, and intermittent IDV with structural change, etc., demands a source-intrinsic origin (e.g., [14–17]).

However, if interpreted as being source-intrinsic, the size of IDV emitting region—through causality and light-travel time arguments—should be less than tens of μ as. This will lead to very high apparent brightness temperature (T_B) that is near or, in many cases, several orders of magnitude in excess of 10^{12} K the inverse-Compton (IC) limit [18]. Thanks to the unprecedented long baseline of the RadioAstron space VLBI, we are able to study the T_B of blazar cores up to 10^{15}–10^{16} K. In fact, the RadioAstron AGN survey program has already discovered T_B well in excess of the inverse-Compton limit in some sources, e.g., $T_B \sim 10^{14}$ K for 3C273 [19]. The cause of the excess—due to high Doppler boosting or a violation of the inverse-Compton limit—remains essentially undetermined. Recent study suggests it may arise from refractive substructure introduced by scattering in the ISM [20].

In this paper, we present a statistical analysis of the IDV of our sample as the first results of the program. We test the dependence of IDV on various source properties and discuss the implications on the origin of IDV.

2. Sample Selection, Observations and Data Reduction

So far, five observing sessions have been carried out at 4.8 GHz. For each session, the main targets were chosen from the RadioAstron block schedule[1]. In order to enable high-precision flux density measurements, a nearby non-variable calibrator was selected for each target based on the result of an IDV survey with the Urumqi 25-m radio telescope ([21], in preparation) as well as a variability survey conducted with the Very Large Array (MASIV survey, [22]). Note that both these two surveys were performed at frequencies close to 4.8 GHz. A few sources of particular interest were occasionally added

---

[1] http://www.asc.rssi.ru/radioastron/schedule/sched.html

to the list as well. With this procedure of source selection, the final source number in each session is ~40, and the total number of sources observed in the whole campaign is 112. However for the statistical analysis in present work, we remove five steep-spectrum calibrators (0836 + 710, 0951 + 699, 3C286, 3C48 and NGC7027) which were observed in all epochs only for calibration purposes. This leaves us with a sample of 107 sources.

Since all the sources are point-like to the beam of the Effelsberg radio telescope at 4.8 GHz, the observations were performed in cross-scan mode, where the antenna beam pattern was driven orthogonally over the source position, stacking four sub-scans for reaching the desired sensitivity. A duty cycle consisted of the observation of the target sources as well as their nearby non-variable secondary calibrators. The average duty cycle is 0.36 h^{-1} in the campaign, which translates into an average time sampling of ~2.8 h for each source.

The basic observing information is summarized in Table 1. In column 1 to 7 we report the epoch designation, starting and ending date, duration, number of sources observed, mean number of flux density measurements per hour, average number of measurements per hour for each source (duty cycle, which represents the shortest time scale on which we can search for IDV), and the average raw modulation index of calibrators which characterizes the systematic uncertainty (see definition in Section 3.1), respectively.

Table 1. Basic information for the five epochs of observing sessions.

Epoch	Date (dd.mm–dd.mm.yyyy)	Duration [*h*]	Number of Observed Sources	Average Sampling [h^{-1}]	Duty Cycle [h^{-1}]	m_c [%]
A	18.07–20.07.2014	62.0	37	14.8	0.40	0.50
B	12.09–15.09.2014	66.6	45	15.9	0.35	0.40
C	31.07–06.08.2015	73.6	42	14.3	0.34	0.40
D	17.12–21.12.2015	82.4	39	14.5	0.37	0.35
E	20.12–24.12.2016	84.4	41	14.0	0.34	0.60

Frequent switching between targets and calibrators allows us to monitor the antenna gain variations with elevation and time, thus improving the subsequent flux density calibration. The data calibration was done in the well-established standard manner, and enabled us to achieve a high precision of flux density measurements (see, e.g., [23]). As the first step of the data calibration, a Gaussian profile is fitted to each sub-scan. The amplitude of the Gaussian is a measure of the source strength, expressed in units of antenna temperature. After applying a correction for small pointing offsets, the amplitudes of all individual sub-scans in one cross-scan are averaged. Subsequently we correct the measurements for the elevation-dependent gain of the antenna and systematic time-dependent effects, using the secondary calibrators close to target sources. Finally, the measured antenna temperature is converted to absolute flux density by a scaling factor determined by utilizing the frequently observed primary calibrators 3C286, 3C48, and NGC7027 [24,25].

The overall error on a single measurement is derived from the formal statistical uncertainty and error propagation in each step of data calibration. The resulting uncertainties usually lie in the range of 0.3–0.7% of total flux density. The result of this calibration procedure can be evaluated by measuring the residual scatter, m_c, of the calibrators (see definition in Section 3.1). For most of the observing sessions, the residual scatter is 0.3–0.5% of total flux density.

With the data calibration procedure described above, the lightcurves of all the observed sources were obtained. In Figure 1 we present an example of lightcurve for the target source 1125 + 596 observed in epoch D. The result of calibrator source 0836 + 710 in the same epoch is superimposed, to demonstrate the stability of the observing system and accuracy of data calibration.
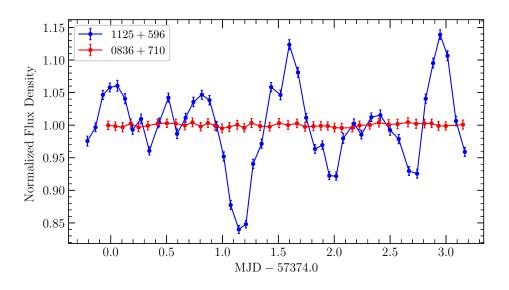
Figure 1. The intra-day variability (IDV) lightcurve (normalized flux density $S / \langle S \rangle$ versus time) of $1125 + 596$ (blue line), and the calibrator $0836 + 710$ (red line) in epoch D.

3. Variability Parameters

A number of parameters are defined to characterize the IDV. For each light curve the 'raw' modulation index m, 'intrinsic' modulation index $\overline{m}$, χ^2, and reduced χ^2 are derived. Here we give a brief definition and description of these quantities, the reader is referred to [26,27] for more details.

3.1. Raw Modulation Index

The raw modulation index is related to the standard deviation of flux density σ and the mean value of flux density $\langle S \rangle$ in the time series by

$$m[\%] = 100 \cdot \frac{\sigma}{\langle S \rangle} \tag{1}$$

and yields a measure for the strength of observed variations. The average value of raw modulation index for all the observed calibrators (m_c) usually represents the calibration accuracy and characterizes the systematic uncertainty.

3.2. Intrinsic Modulation Index

The intrinsic modulation index [27] is an alternative estimator to quantify the variability that would be observed in the absence of measurement errors with ideal time sampling. Note that this use of 'intrinsic' is not referring to source-intrinsic variability, but includes any intrinsic and extrinsic (ISS-induced) variations in the received flux density.

With the assumption that the 'true' flux densities for each source are normally distributed with mean S_0, standard deviation σ_0, and intrinsic modulation index $\overline{m} = \sigma_0 / S_0$, the probability density for the true flux density S_t is

$$p(S_t, S_0, \sigma_0) = \frac{1}{\sigma_0 \sqrt{2\pi}} \exp \left[-\frac{(S_t - S_0)^2}{2\sigma_0^2} \right] . \tag{2}$$

Furthermore, we assume that the observation process for the jth data point adds normally distributed error with mean S_t and standard deviation σ_j. Then the likelihood for a single observation is given by

$$\ell_j(S_0, \sigma_0) = \int_{\text{all } S_t} dS_t \, \frac{\exp\left[-\frac{(S_t - S_j)^2}{2\sigma_j^2}\right]}{\sigma_j \sqrt{2\pi}} \frac{\exp\left[-\frac{(S_t - S_0)^2}{2\sigma_0^2}\right]}{\sigma_o \sqrt{2\pi}}, \tag{3}$$

which after combining $j = 1, ... N$ measurements and substituting $\overline{m} S_0 = \sigma_0$, gives

$$\mathcal{L}(S_0, \overline{m}) = S_0 \left(\prod_{j=1}^{N} \frac{1}{\sqrt{2\pi \left(\overline{m}^2 S_0^2 + \sigma_j^2 \right)}} \right) \exp\left(-\frac{1}{2} \sum_{j=1}^{N} \frac{(S_j - S_0)^2}{\overline{m}^2 S_0^2 + \sigma_j^2} \right). \tag{4}$$

By maximizing the joint likelihood given by Equation (4), we find our estimates of S_0 and $\overline{m}$.

The maximum-likelihood we applied makes the assumption that distribution of flux densities from a source is distributed normally. For many sources, this is a good description of the data. As an example, in the left panel of Figure 2, we plot the histogram of epoch D data set flux densities from 1125 + 596 (for which the IDV curve is shown in Figure 1). It is clear that the histogram approximately forms a Gaussian profile. In the right panel of Figure 2, we plot the most likely values and the 1σ, 2σ, and 3σ isolikelihood for the same source. The contours were computed to contain 68.26%, 95.45%, and 99.73% of the volume beneath the likelihood surface. In this way, we obtained the most likely values of $\overline{m}$ and S_0, as well as their 1σ uncertainties. We note that a rigorous estimate of the uncertainty in individual $\overline{m}$ is essential for evaluating the significance of differences between $\overline{m}$ through population studies which will be demonstrated in Section 5.
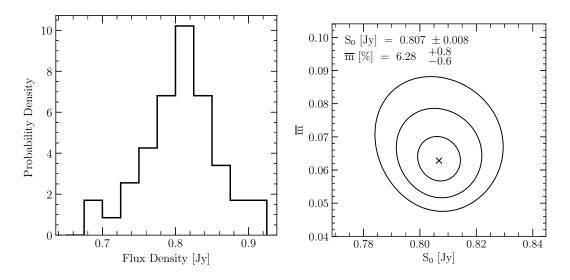

Figure 2. Maximum likelihood estimation for blazar 1125 + 596 observed in epoch D. (**Left**) Distribution of measured flux density. (**Right**) 1σ, 2σ, and 3σ contours of the joint likelihood $\mathcal{L}(\overline{m}, S_0)$.

3.3. χ^2 and Reduced χ^2

Finally, as a criterion to identify the presence of variability, the null-hypothesis of a constant function is examined via a χ^2-test

$$\chi^2 = \sum_{j=1}^{N} \left(\frac{S_j - \langle S \rangle}{\sigma_j} \right)^2 \tag{5}$$

and the reduced value of χ^2

$$\chi_r^2 = \frac{1}{N-1} \sum_{j=1}^{N} \left(\frac{S_j - \langle S \rangle}{\sigma_j} \right)^2 \tag{6}$$

A source is classified as variable if the χ^2-test gives a probability of <0.01% for the assumption of constant flux density (99.99% significance level for variability).

4. Statistical Results

Table A1 summarizes the basic properties and statistical results of sources in the sample. Columns 1 and 2 give the source name and epoch designation. Observation results are presented in columns 3, 4, and 5. Column 6 gives variability classification. A '+' is given if the source is identified as variable. Source-basic properties, i.e., galactic latitude, spectral index, redshift, VLBI core size at 5 GHz, and core-dominance, are shown in column 7–11, respectively. Column 12 lists the γ-ray loudness. A '+' is marked if the source is included in the Fermi Large Area Telescope Third Source Catalog (3FGL, [28]). The galactic latitudes and redshifts were taken from the NASA/IPAC Extragalactic Database (NED[2]) and spectral indexes (defined by $S \propto \nu^\alpha$ where S the flux density and ν the observing frequency) from the Radio Fundamental Catalog[3]. The VLBI core sizes were extracted from [29]. The core-dominance, defined by $f_c = S_{core}/S_{total}$, was derived by use of data from the Radio Fundamental Catalog.

In the following we overview the statistical properties of the sample. We present the distributions of source flux density, spectral index, galactic latitude, and intrinsic modulation index. For the purpose of population study, the distribution of $\overline{m}$ is analytically modeled.

4.1. Variability Classification

To verify the presence of IDV, a χ^2-test is applied to each observed lightcurve. Of the 107 targets observed, 31 sources are found to exhibited IDV in at least one observing epoch, while the rest of the sample does not reveal evident IDV in any epoch. This leads to an IDV detection rate of ~30% for current sample, comparable to earlier studies [6,7]. In order to minimize the chance of misclassification, a cross-check of the intrinsic modulation index is performed alternatively. If the maximum-likelihood $\overline{m}$ is less than 3σ away from $\overline{m} = 0$, we consider that significant variability cannot be established in the source. As a result, the new approach classifies three extra sources as variable, besides the 31 IDV sources previously identified by χ^2 tests. The result demonstrates that our variability verification with different approaches are mostly consistent with each other. In Figure 3 we show a scatter plot of the intrinsic modulation index $\overline{m}$ of all sources against their mean flux density, using different symbols for variables and non-variables identified with both approaches. A dashed horizontal line at $\overline{m} = 0.75\%$ roughly separates the variable from non-variable classifications, confirming the result of the χ^2-test.

4.2. Sample Properties

An overview of the sample properties is presented in Figure 4. In each panel, IDV sources are plotted in red and non-IDVs in blue. The distribution of flux density is plotted in panel (a), showing a bimodal profile for non-IDVs. It is obvious that IDV sources are mostly clustered at the lower flux density peak, while the higher flux density peak is predominantly occupied by the non-IDV population. Panel (b) shows the unimodal distribution of spectral index. The variables are well distributed at $\alpha > -0.1$, indicating deviation from the non-variable population. In panel (c) the source galactic latitude shows a distribution peaked at $|b|$ ~35°. The occurrence of IDV and non-IDV sources reveals a similar trend, and no clear difference can be visually observed between these two populations. We note that sources with $|b| < 10°$ are very rare in our sample. The occurrence of IDV/non-IDV among γ-ray loud and γ-ray quiet subsamples is compared in panel (d). Of the 63 sources with a GeV detection by Fermi, 25 exhibit IDV, indicating that ~40% of the γ-ray loud sources are variable at cm-wavelength. By contrast the ratio is as low as ~14% for γ-ray quiet sources, indicating a higher occurrence rate of IDV in γ-ray loud population.

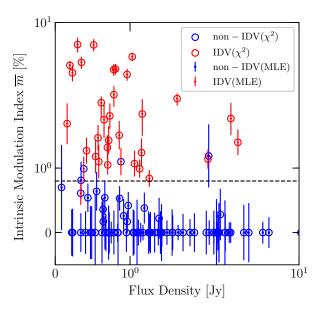[2]   https://ned.ipac.caltech.edu/
[3]   http://astrogeo.org/rfc/

Figure 3. Intrinsic modulation index $\overline{m}$ plotted against mean flux density. Sources classified as variables are plotted in red while non-variables are in blue. Classification with χ^2-test (χ^2) plotted as circles while maximum likelihood estimation (MLE) is shown as an error bar.
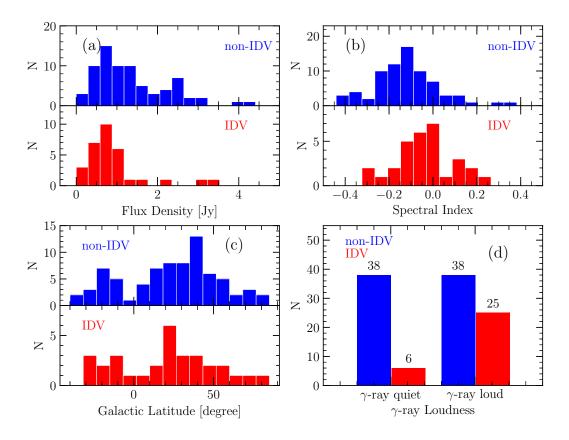

Figure 4. Sample properties. Panels (**a**–**d**) present the distribution of flux density, spectral index, galactic latitude, and γ-ray loudness, respectively. In each panel, IDV sources are plotted in red and non-IDVs in blue.

4.3. Intrinsic Modulation Index $\overline{m}$

The probability density of $\overline{m}$ for our monitoring sample is plotted in Figure 5. As in [27,30], we use a monoparametric exponential family of distributions

$$f(\overline{m})d\overline{m} = \frac{1}{m_0} \exp(-\frac{\overline{m}}{m_0})d\overline{m} \qquad (7)$$

with mean m_0 to model the observed probability density of $\overline{m}$. The red line represents the best fit with mean $m_0 = 0.63\%$ in the form of Equation (7). The model, which provides an excellent description of the data, will be used to characterize various subgroups of our sample, as we will see in the next section. We note that a median value of $\overline{m}$ is adopted if the source was observed in multiple epochs. The robustness of the population comparisons presented in Section 5 will be discussed in Section 6.
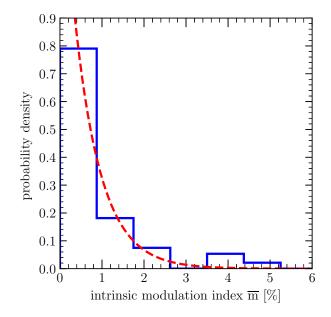

Figure 5. Probability density of the maximum-likelihood intrinsic modulation indexes $\overline{m}$. The red dashed line represents an exponential distribution with $m_0 = 0.63\%$.

5. Population Comparisons

We now investigate how the variability amplitude, as quantified by $\overline{m}$, depends on source properties, i.e., flux densities, spectral indexes, γ-ray loudness, and galactic latitudes. To this end, we determine the distribution of $\overline{m}$ for various subsets of our sample with, again, a likelihood maximization method as in [27].

The likelihood analysis requires a parent distribution for $\overline{m}$. As shown in Section 4.3, an exponential distribution as given in Equation (7), is a qualitatively reasonable fit to the observed distribution of modulation indexes in our sample. Under the assumption that the exponential distribution (Equation (7)) is the correct underlying distribution for $\overline{m}$ in any given subset (i.e., population) of our source sample, we can use the parameter m_0 as a measure for the population to show strong IDV. To find m_0, we perform a likelihood analysis, as described in Section 5.1. We hereby use the maximum of the normalized likelihood function to determine m_0 for each population, or rather we investigate the probability distribution of any possible m_0 values to estimate the statistical significance of differences in m_0 found for different populations.

We also performed *k*-sample Anderson–Darling (A-D) tests [31] to each pair of subsamples for crosschecking. The A-D test is a nonparametric statistical procedure testing the hypothesis that the populations from which two or more samples of data were drawn to be identical. It is a modification of the Kolmogorov–Smirnov (K-S) test and gives more weight to the tails than does the

latter, thus allowing a more sensitive test for exponential-like distribution and offering a better option for the statistics in current study.

5.1. Likelihood Analysis

Here we briefly introduce the methodology of maximum-likelihood used for population studies in this work. More details can be found in Section 6.3.3 of [27] where the formalism is well demonstrated.

For a source i, the likelihood of observing a modulation index $\overline{m}_i$ with a Gaussian uncertainty σ_i drawn from an exponential distribution with mean m_0 is

$$
\begin{aligned}
\ell_i(m_0) &= \int_{\overline{m}=0}^{\infty} d\overline{m} \frac{1}{m_0} \exp\left(-\frac{\overline{m}}{m_0}\right) \frac{1}{\sigma_i\sqrt{2\pi}} \exp\left[-\frac{(\overline{m}-\overline{m}_i)^2}{2\sigma_i^2}\right] \\
&= \frac{1}{m_0\sigma_i\sqrt{2\pi}} \exp\left[-\frac{\overline{m}_i}{m_0}\left(1-\frac{\sigma_i^2}{2m_0\overline{m}_i}\right)\right] \times \int_{\overline{m}=0}^{\infty} \exp\left[-\frac{[\overline{m}-(\overline{m}_i-\sigma_i^2/m_0)]^2}{2\sigma_i^2}\right] d\overline{m},
\end{aligned}
\tag{8}
$$

where, to obtain the second expression, we have completed the square in the exponent of the integrand. The last integral can be calculated analytically, yielding

$$
\ell_i(m_0) = \frac{1}{2m_0} \exp\left[-\frac{\overline{m}_i}{m_0}\left(1-\frac{\sigma_i^2}{2m_0\overline{m}_i}\right)\right] \times \left\{1 + \mathrm{erf}\left[\frac{\overline{m}_i}{\sigma_i\sqrt{2}}\left(1-\frac{\sigma_i^2}{m_0\overline{m}_i}\right)\right]\right\}.
\tag{9}
$$

The likelihood of N observations of this type is

$$
\mathcal{L}(m_0) = \prod_{i=1}^{N} \ell_i(m_0).
\tag{10}
$$

The probability density function (PDF) of m_0 is the normalization of $\mathcal{L}(m_0)$,

$$
\mathrm{pdf}(m_0) = \frac{\mathcal{L}(m_0)}{\int_0^{\infty} \mathcal{L}(m_0)\,dm_0}
\tag{11}
$$

From the maximization of Equation (11) we obtain the maximum-likelihood value of m_0. The statistical uncertainty (1σ error) on this value can also be obtained by locating the isolikelihood m_0-values m_{01} and m_{02} for which

$$
\mathrm{pdf}(m_{01}) = \mathrm{pdf}(m_{02})
\tag{12}
$$

and

$$
\frac{\int_{m_{01}}^{m_{02}} \mathrm{pdf}(m_0)dm_0}{\int_0^{\infty} \mathrm{pdf}(m_0)dm_0} = 0.6826.
\tag{13}
$$

The confidence intervals are derived in a similar way by substituting the right-hand side of Equation (13) by, e.g., 0.9545 and 0.9973 for the cases of 2σ and 3σ, respectively. We note that the 1σ errors and confidence intervals for the difference of m_0 are calculated in the same way.

With the above introduced formalism, we are able to examine whether the intrinsic modulation index $\overline{m}$ correlates with the properties of the sources in our sample. In the following sections, we will study the distributions of $\overline{m}$-values in the subgroups of our monitoring sample according to some source properties, i.e., flux densities, spectral indexes, γ-ray loudness, and Galactic latitudes as well.

A summary of population comparisons between various subsamples is tabulated in Table 2. For each subsample, in column 1 we list the criteria used for subsample division; in column 2 we present the number of sources in subsample; in column 3 we estimate the most likely values of m_0 by maximizing the likelihood function given in Equation (11). The associated 1σ uncertainties are also provided. For each pair of subsamples compared, in column 4 we calculate the most likely value along with the corresponding 1σ uncertainties for the difference in m_0; in column 5 we list the significance

of the difference. Finally, the *p*-value and significance as estimated from A-D tests are reported in Column 6 and 7, respectively. As shown in the table, the results from two statistical approaches are highly consistent with each other.

Table 2. Results of population comparisons.

Subsample	Source Num.	Likelihood Analysis			Anderson–Darling Test	
		m_0 [%]	Δm_0 [%]	Significance	p	Significance
$S_{4.8} < 1$ Jy	53	$1.24^{+0.198}_{-0.165}$	$+0.78^{+0.205}_{-0.187}$	5σ	1.32×10^{-5}	4σ
$S_{4.8} \geq 1$ Jy	54	$0.46^{+0.077}_{-0.064}$				
$\alpha < -0.1$	51	$0.59^{+0.102}_{-0.084}$	$-0.47^{+0.172}_{-0.189}$	3σ	5.23×10^{-4}	3σ
$\alpha \geq -0.1$	56	$1.07^{+0.167}_{-0.139}$				
γ-ray quiet	44	$0.43^{+0.082}_{-0.067}$	$-0.69^{+0.162}_{-0.179}$	4σ	4.37×10^{-4}	3σ
γ-ray loud	63	$1.13^{+0.164}_{-0.139}$				
$|b| < 20°$	34	$0.98^{+0.206}_{-0.163}$	$+0.18^{+0.229}_{-0.194}$	$<1\sigma$	9.67×10^{-1}	$<1\sigma$
$|b| \geq 20°$	73	$0.79^{+0.107}_{-0.091}$				

5.2. Flux Density and Redshift

In order to exhibit ISS, a source must contain a component that is sufficiently compact, with angular diameter comparable to or smaller than the first Fresnel zone of the scattering screen, i.e., on the order of tens of μ as near a few GHz (e.g., [12,32,33]).

We start with testing the dependence of IDV on source flux density, which is tightly bounded with source angular size if the brightness temperature is inverse-Compton limited. A population study is also performed to examine the subsets defined by whether the source flux density is higher or lower than 1 Jy. The results of this test are displayed in Figure 6. In the left panel, it is obvious that the curves for the two subsamples are not consistent with each other – weaker sources have, on average, higher IDV amplitude. The significance of this result is verified by the right panel of Figure 6, where we plot the probability density of the difference between the m_0 of the two subsets (which is formally equal to the cross-correlation of their individual distributions). With the formalism introduced in Section 5.1 the most likely difference is 0.84 percentage of points, which is more than 5σ away from zero. Our result can be understood in terms of source angular scale. The angular size of a source can be modeled as a function of its flux density, *S*, and the brightness temperature T_B in source frame, as follows:

$$\theta = \sqrt{\frac{\lambda^2(1+z)S}{2\pi k \delta T_B}}, \tag{14}$$

where λ is the observing wavelength, *z* is the source redshift, *k* is the Boltzmann constant, and δ is the Doppler boosting factor. Therefore, if these sources are limited in brightness temperature, either due to the inverse-Compton catastrophe [18] or energy equipartition (between particles and the magnetic fields [34]), the source angular size scales as $\theta \propto S^{0.5}$. In that case, the brighter sources have larger angular sizes, and thus suppress the ISS. In other words, our finding indicates a source compactness related IDV. Moreover, with the availability of VLBI data on the core size (column 10 of Table A1), it is possible to verify the argument by testing the correlation between intrinsic modulation index and VLBI core size at 5 GHz directly. The two-tailed, non-parametric Spearman rank correlation test gives a correlation coefficient $r_s = -0.219$ and a *p*-value of $p = 6.44 \times 10^{-2}$. Though it is less significant, a negative trend in the IDV strength over source angular size is implied.

Furthermore, the observed IDV may be also dependent on the source redshift, providing that the sample of sources are both flux density- and brightness temperature-limited [7]. In this case the redshift dependence of the angular size is $\theta \propto (1+z)^{0.5}$ due to cosmological expansion. However we do not

find a statistically significant relation between redshift and IDV amplitudes in our sample. We note that the scatter in flux density is larger than the scatter in $(1 + z)$, and there is no clear relationship seen between source flux density and redshift in this sample. Moreover, a suppression of ISS was observed in the MASIV survey only for sources with $z > 2.5$ [7]. Our sample has only four sources with $z > 2.5$.
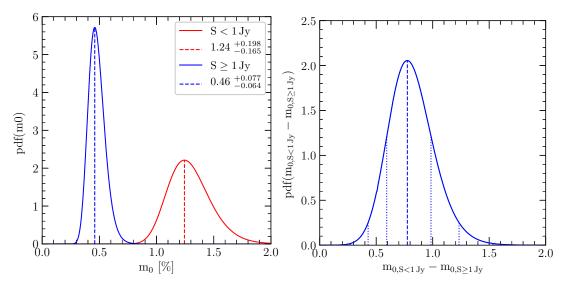

Figure 6. (**Left panel**) Probability density of m_0 for sources with flux density lower (red solid line, maximum-likelihood value and 1σ error $m_0 = 1.24^{+0.198}_{-0.165}\%$) and higher (blue solid line, maximum-likelihood value and 1σ error $m_0 = 0.46^{+0.077}_{-0.064}\%$) than 1 Jy in our monitoring sample. The dashed vertical lines locate the peaks of probability density for the two subsamples. (**Right panel**) Probability density of the difference between the m_0 for the two sets considered in the left panel. The dashed vertical line shows the peak of the probability density, while the dotted vertical lines represent the 1, 2, and 3σ confidence interval. The peak of the distribution ($0.78^{+0.205}_{-0.187}$) is over 5σ away from zero.

5.3. Spectral Index

Early observations showed that scintillating sources tend to have flat or inverted spectra, while the steep-spectrum radio sources do not scintillate [35]. This can be understood by considering that the flat-spectrum sources are dominated by optically thick, synchrotron self-absorbed components with very high-brightness temperature, and thus most of their flux density is confined to the ultra-compact core region. In contrast, the steep-spectrum sources are dominated by optically thin, less compact components with lower brightness temperatures, often related to an extended VLBI jet.

To test this argument, we split the sample at $\alpha = -0.1$. This criterion roughly splits our sample into flat and inverted spectra, and produces subsamples of similar numbers of objects. Figure 7 depicts the probability distributions of m_0 as well as the difference between m_0 for the two subsamples. A Spearman rank test between the intrinsic modulation index and source core-dominance (column 11 of Table A1) confirms the result ($r_s = 0.284$ and $p = 9.72 \times 10^{-3}$). The finding, as anticipated, suggests that sources with inverted spectra are significantly stronger in short-term variability. It has to be noted, however, that the sources in the present sample are mostly compact, core-dominated sources with flat spectrum, unlike the classical steep-spectrum sources reported by Heeschen [35] which are dominated by their extended emission. Our findings indicate that even within the flat spectrum sources the presence of additional less compact components could in principle reduce their core-dominance, thus reducing the scintillation.

5.4. γ-Ray Loudness

The source of high energy emission is believed to be compact and located close to the central engine of AGNs (e.g., [36,37]). Relations between the parsec-scale radio properties and γ-rays of blazars have been intensively investigated since the Fermi γ-ray Space Telescope was launched (e.g., [38–41]). In this study we test, through a statistical approach, whether there is a correlation between the γ-ray loudness and the 4.8 GHz IDV properties.
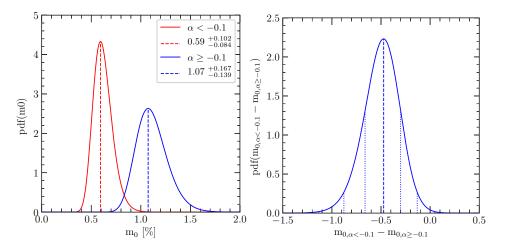

Figure 7. Similar to Figure 6 but for sources with spectral index lower (red solid line) and higher (blue solid line) than -0.1. In the left panel the maximum-likelihood value and the associated 1σ error are indicated in the legend. In the right panel the peak of the distribution ($-0.47^{+0.172}_{-0.189}$) is over 3σ away from zero.

We thus divide our sample in two subsets, based on whether the source has been detected by Fermi LAT at a significance level high enough to warrant inclusion in the 3FGL catalog. As shown in Figure 8, these two subsamples reveal different properties: the γ-ray loud sources have, on average, an IDV amplitude almost a factor of four higher than γ-ray quiet ones. The result is very significant statistically, with the maximum-likelihood difference being 4σ away from 0, as indicated in the right panel of Figure 8.

We further investigated the possible relation between the integrated γ-ray photon flux and the radio flux density at 4.8 GHz. The γ-ray fluxes have been extracted from the 3FGL catalog [28] and are averaged over the entire operational time of Fermi satellite. The 4.8 GHz measurements are averaged over a few days and hence are most likely free of long-term variability. Our analysis showed that the two are likely correlated. In the case of photon fluxes in the range 100–300 MeV, the Spearman correlation coefficient turns out to be $r_s = 0.46$ with $p = 1.36 \times 10^{-4}$. In the case of fluxes in the range 1–100 GeV the correlation weakens, with r_s being around 0.37 and a p-value of 3.15×10^{-3}. These numbers show that the radio flux density (which is an indicator of source compactness and brightness temperature) and γ-ray photon flux are significantly correlated.

5.5. Galactic Latitude

We have also investigated the dependence of the IDV at the galactic latitude. In the case of ISS, a galactic latitude dependence of IDV is anticipated, since the diffuse interstellar medium (ISM) is mostly distributed near the Galactic plane. A contingency test by dividing the sample into low and high galactic latitude subsamples at $|b| = 20°$ reveals that although the low galactic latitude subsample on average exhibits marginally higher IDV amplitudes than that at high galactic latitude, the two distributions of m_0 are rather consistent with each other statistically. The probability density for the difference between m_0 for the two subsamples is consistent with zero to within 1σ (see Figure 9).
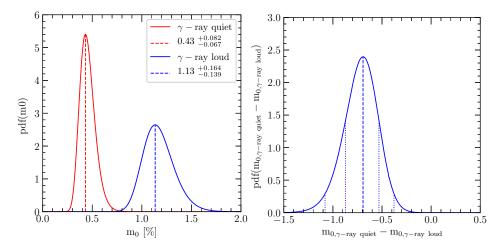
Figure 8. Similar to Figure 6 but for γ-ray quiet (red solid line) and γ-ray loud (blue solid line) sources. In the left panel the maximum-likelihood value and the associated 1σ error are indicated in the legend. In the right panel the peak of the distribution ($-0.69^{+0.162}_{-0.179}$) is ~4σ away from zero.

In order to further verify this result, we then compare the IDV strength with the Galactic foreground emission measure (column density of the square of the electron density) as estimated from observations of Hα emission (i.e., the Wisconsin Hα Mapper Northern sky survey, WHAM [42]). The integral Hα intensity (in rayleighs) integrated over all velocities is believed to be proportional to the ISM emission measure in the line of sight, providing that the temperature of the emitting gas does not vary by a large percentage. By finding the integrated Hα intensity from the WHAM nearest to each source, we are able to test the correlation between the IDV strength and the emission measure along the line of sight. We find no significant correlation between Hα intensity and modulation index; the Spearman correlation gives $r_s = 0.180$ and $p = 6.43 \times 10^{-2}$.

Previous studies with larger source samples suggest a significant variability dependence on Galactic latitude (e.g., [7,43,44]). A recent statistical study on AGN cores reveals that the effect of angular broadening by ISM scattering is significant only for sources at low galactic latitude (i.e., $|b| < 10°$) [29]. Given the fact that only 12 of our sources are at low galactic latitudes $|b| < 10°$, the lack of such a dependence in the current study might be simply ascribed to this small number.
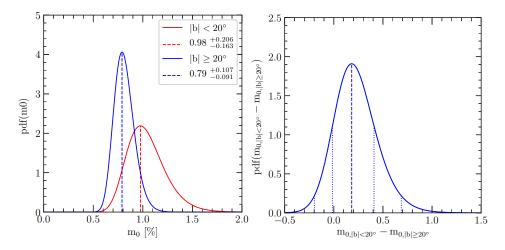

Figure 9. Similar to Figure 6 but for low (red solid line) and high (blue solid line) galactic latitude sources in our sample. In the left panel the maximum-likelihood value and the associated 1σ error are indicated in the legend. In the right panel the peak of the distribution ($0.18^{+0.229}_{-0.194}$) is consistent with zero within 1σ.

6. Discussion

6.1. Robustness of the Statistics

A considerable portion of the sample was observed at multiple epochs. In that case, median values of source flux density and intrinsic modulation index are adopted for the statistical analysis presented in current study. To evaluate a possible bias introduced by the median-value selection approach for duplicate observations, both the minimum-value and maximum-value selection are tested. For simplicity we hereafter refer to these two selection approaches as TMIN and TMAX, respectively.

The distributions of intrinsic modulation index, for both TMIN and TMAX, show similar trends to that of the median-$\overline{m}$ selection, and can be characterized by an exponential distribution given in Equation (7), with $m_0 = 0.62\%$ and 0.66%, respectively. The variability strengths for various subsamples are re-analyzed and compared by using the methodology demonstrated in Section 5. The results are listed in Table 3. Though the estimated m_0 and Δm_0 values are systematically lower for TMIN and higher for TMAX, the significances are comparable. The consistency between these results indicates that our previous findings on IDV dependence hold true even with 'extreme' selection approaches on $\overline{m}$.

Table 3. Results of population comparisons with minimum- and maximum-$\overline{m}$ selection.

Subsample	TMIN			TMAX		
	m_0 [%]	Δm_0 [%]	Significance	m_0 [%]	Δm_0 [%]	Significance
$S_{4.8} < 1\,\mathrm{Jy}$ $S_{4.8} \geq 1\,\mathrm{Jy}$	$1.11^{+0.178}_{-0.148}$ $0.46^{+0.078}_{-0.065}$	$+0.65^{+0.186}_{-0.172}$	4σ	$1.48^{+0.237}_{-0.197}$ $0.48^{+0.080}_{-0.066}$	$+0.99^{+0.220}_{-0.236}$	5σ
$\alpha < -0.1$ $\alpha \geq -0.1$	$0.58^{+0.099}_{-0.082}$ $0.97^{+0.151}_{-0.126}$	$-0.39^{+0.160}_{-0.173}$	3σ	$0.61^{+0.104}_{-0.086}$ $1.30^{+0.202}_{-0.169}$	$-0.68^{+0.198}_{-0.222}$	4σ
γ-ray quiet γ-ray loud	$0.41^{+0.079}_{-0.064}$ $1.05^{+0.152}_{-0.128}$	$-0.62^{+0.150}_{-0.168}$	4σ	$0.45^{+0.085}_{-0.069}$ $1.34^{+0.194}_{-0.164}$	$-0.88^{+0.184}_{-0.209}$	5σ
$|b| < 20°$ $|b| \geq 20°$	$0.89^{+0.188}_{-0.148}$ $0.74^{+0.101}_{-0.086}$	$+0.14^{+0.212}_{-0.178}$	$<1\sigma$	$1.17^{+0.248}_{-0.195}$ $0.88^{+0.119}_{-0.102}$	$+0.28^{+0.267}_{-0.233}$	1σ

6.2. Variability Dependencies

A strong dependence of IDV on source flux density is found in our sample. A similar effect was also observed in the MASIV survey [22], where an increase in fractional amplitude of IDV with decreasing flux density was observed. The result raised the possibility that the milliarcsecond-scale structures of the IDV sources may differ from those of non-IDVs, in the sense that the weaker sources are more compact. Consistent with this result, a direct comparison of milliarcsecond source structures between IDV/non-IDV sources showed that the former typically have smaller size than the latter [45]. Moreover, the ISS-induced variability leads us to expect a flux density-dependent IDV, being common in compact objects but rare in objects with bright VLBI-scale jets (e.g., [6,22]). This is also the case for our sample, in which the fractional occurrence of IDV is ~40% and ~18% for the weak and strong subsamples, respectively. The finding that IDV amplitude depends on the total flux density implies that the low flux-density sources identified in our sample are more compact.

It has long been suggested that flat-spectrum sources are more likely to show IDV [5] than steep-spectrum sources. We narrow that conclusion by finding that in our selection of flat-spectrum sources, those with inverted spectra, on average, show stronger variability than sources with other spectral shapes. Since the flux density of inverted spectrum sources is more 'core dominated', our results strongly support the model that it is the most compact and core-dominant component of the blazars that causes IDV due to scintillation through the ISM.

We found a significant IDV dependence on γ-ray loudness in our sample. Prior to discussing the physical implications from this dependence, it is essential to discern the possible correlation between

spectral indexes and γ-ray loudness, e.g., to test whether the γ-ray loud population is also dominated by inverted-spectrum sources.

The K-S and A-D tests reveal that the distribution of the spectral index for γ-ray loud and γ-ray quiet sources is significantly different ($p_{K-S} = 5.49 \times 10^{-4}$ and $p_{A-D} = 1.34 \times 10^{-3}$ for K-S and A-D tests, respectively), with the γ-ray loud sample being dominated by the more inverted-spectrum sources. As mentioned above, the inverted-spectrum sources are dominated by optically thick compact components with higher brightness temperatures than their flat-spectrum counterparts. For such sources the energy of radiative particles dominates over that of the magnetic field, and inverse-Compton (IC) scattering is therefore more efficient. This leads to an increased production of γ-rays if IC scattering is the dominant γ-ray emission process. Another possibility is that the inverted spectrum (thus more core-dominated) sources are more strongly beamed (e.g., [46]). In that case, as their apparent flux density is more strongly Doppler-boosted, for a given intrinsic brightness temperature they will have smaller angular sizes. Thus, they are more likely to scintillate and they are also more likely to have detectable γ-ray emission, which is dependent on beaming (e.g., [47]). Furthermore, a positive correlation between the 4.8 GHz radio flux density and the γ-ray photon flux is found, which supports the view that it is the radio photons from the synchrotron branch of the spectral energy distribution (SED) that are up-scattered by the inverse-Compton process to the higher energies.

Our findings indicate a strong connection between the origin of radio and γ-ray emission. While the radio emission of blazars is believed to be produced by synchrotron emission of relativistic electrons, which is Doppler-boosted, the origin of the γ-ray emission is still controversial, especially with regard to the target photon field and the location of the emission site (see, e.g., [48–50]). Besides these leptonic models there are also models where the γ-rays originate from hadronic processes, i.e., relativistic protons co-accelerated with the electrons (e.g., [51]). In this case, rather strong magnetic fields would be required. Following [52], the typical magnetic field strength for the sources in our sample can be calculated. Due to the lack of detailed spectral information for the scintillating component, we adopt a typical spectral turnover frequency near 15 GHz from a recent statistical study of AGN jet compactness and brightness temperatures ([53], see Figure 1). For a source with an angular size of the order of the scattering size $\theta = 0.05{\sim}0.25$ mas, a typical peak flux density $S_m = 1$ Jy, and Doppler factor $\delta = 10$, one obtains a magnetic field strength of 1.7 mG~1.1 G, which would favor leptonic models, unless the turnover frequency or the Doppler factor would be much higher. Dedicated future studies will be necessary to further explore this topic.

The presence of a relationship between ISS and galactic latitude has long been suggested from previous surveys (e.g., [7,43,44]). However, in this study only a marginal dependence was observed. Besides the smaller size of the sample as discussed in Section 5.5, the lack of a clear correlation may indicate that it is predominantly the intrinsic properties (e.g., angular size, core-dominance) of the blazars that determine how they scintillate, rather than properties of the distributed ISM. In other words, a sufficiently compact source is likely to show IDV, no matter through which part of the Galaxy it is observed. This statement excepts intra-hour variability (e.g., [8,11,33]), an extremely rare ($\ll$1%) phenomenon that requires an unusually nearby screen.

The ISM is known to be highly inhomogeneous with small-scale discrete structures, such as photon-dominant regions (PDRs, e.g., [54]), high-latitude clouds (HLCs, e.g., [55]), local interstellar clouds (LICs, e.g., [56]), and ionized flows driven by nearby hot stars (e.g., [57]), etc. Such structures may dominate over the more diffuse ISM on the galactic latitude dependence of IDV: local structures within ~100 pc of the Sun can produce the strongest and most rapid IDV, due to the angular size of the first Fresnel zone scaling with the inverse square root of screen distance. Scintillation from more distant scattering screens is averaged out over the finite angular diameter of the source. The high occurrence rate of IDV in compact radio sources indicates that for many AGN, the line-of-sight intersects such inhomogeneities.

6.3. Influence on SVLBI T_B Measurements

RadioAstron blazars that are strongly core-dominated should show significant IDV due to ISS, with the largest modulations expected near 5 GHz (e.g., [7]). To account for the effects of ISS during the RadioAstron observations, coordinated flux density monitoring over an extended period is necessary. To estimate the uncertainties of the T_B measurements obtained from SVLBI and influenced by rapid flux variations, we assume that the source has a VLBI core component containing all the variable flux. We approximate this component with a circular Gaussian. The relation between visibility and angular diameter of this Gaussian is expressed as [58]

$$F(\rho) = \exp\left(\frac{-(\pi\theta\rho)^2}{4\ln 2}\right)$$ (15)

where θ is the angular diameter and ρ the baseline length. The uncertainty of θ is given by

$$\Delta\theta = -\frac{\overline{m}}{2} \cdot \frac{\sqrt{1+f_c^{-2}}}{\ln f_c} \cdot \theta$$ (16)

in which $\overline{m}$ the intrinsic modulation index and $fc = S_{core}/S_{total}$ the core-dominance. Analytically applying the error propagation, one obtains for the uncertainty of T_B

$$\Delta T_B = \overline{m} \cdot \left(1 + \frac{1+f_c^{-2}}{\ln^2 f_c}\right)^{1/2} \cdot T_B$$ (17)

which leads to an uncertainty of ~70% in T_B for a source which varies with $\overline{m} = 10\%$ and whose core dominance is $f_c = 0.8$.

7. Summary and Conclusions

We presented statistical results based on five observing sessions of an IDV monitoring program with the Effelsberg 100-m radio telescope at 4.8 GHz. The overall statistics of the observed AGN showed that 31 out of 107 sources exhibited IDV, leading to an IDV detection rate of ~30%. The IDV occurrence for γ-ray loud sources is ~40%, which is significantly higher than that for the γ-ray quiet ones.

Moreover, with a maximum-likelihood approach we investigated the IDV dependence on various sources properties and on the galactic latitude. We found significant differences in the strength of IDV, dependent on the source flux density, spectral index and γ-ray loudness. The results show that, weak (S < 1 Jy), inverted spectrum ($\alpha > -0.1$), or γ-ray loud sources, on average, exhibit significantly stronger IDV (significance > 3σ). On the other hand, we did not find a significant dependence of IDV on the galactic latitude, which may suggest that it is predominantly the intrinsic properties (e.g., angular size, core-dominance) of the blazars that determine how they scintillate, rather than the directional dependence in the ISM. We estimate that for the blazars which show strong IDV, the uncertainty in the observed VLBI brightness temperature can be as high as ~70%. A better physical understanding of these findings should become possible from direct size measurements through the ongoing RadioAstron space VLBI observations.

Appendix A. Results of IDV Monitoring with the Effelsberg 100 m Telescope

Table A1. Source properties and statistical results of Effelsberg monitoring (see Section 4 for detailed description).

Name	Epoch	Flux Density [Jy]	$\overline{m}$ [%]	χ^2_r	IDV	b [°]	α	z	θ_5 [mas]	f_c	γ-ray
0010 + 405	B	0.976 ± 0.002	$0.42^{+0.24}_{-0.21}$	1.586		−21.44	−0.24	0.255	0.70	0.78	
0014 + 813	B	1.642 ± 0.002	$0.00^{+0.12}_{-0.12}$	0.133		18.80	−0.01	3.366	0.63	0.75	
0016 + 731	B	2.106 ± 0.005	$1.14^{+0.23}_{-0.15}$	4.485	+	10.73	−0.13	1.781	0.57	0.79	
0059 + 581	A	3.517 ± 0.011	$1.40^{+0.31}_{-0.20}$	2.607	+	−4.44	−0.06	0.644	0.61	0.66	+
0110 + 318	C	0.650 ± 0.002	$0.00^{+0.61}_{-0.61}$	1.047		−30.51	−0.30	0.603			+
	D	0.697 ± 0.002	$1.32^{+0.30}_{-0.19}$	4.053	+						
	E	0.814 ± 0.003	$0.00^{+0.42}_{-0.42}$	0.214							
0125 + 487	B	0.341 ± 0.001	$0.61^{+0.25}_{-0.18}$	1.935		−13.41	+0.27	0.067			
0219 + 428	D	1.191 ± 0.002	$0.38^{+0.24}_{-0.24}$	1.175		−16.77	−0.22	0.444	1.83	0.42	+
0234 + 285	E	2.547 ± 0.009	$0.00^{+0.46}_{-0.46}$	0.459		−28.53	−0.17	1.213		0.44	+
0235 + 164	E	2.133 ± 0.010	$1.19^{+0.59}_{-0.49}$	1.720		−39.11	+0.01	0.940	0.65	0.88	+
0248 + 430	D	0.860 ± 0.001	$0.53^{+0.24}_{-0.19}$	1.411		−14.40	−0.18	1.310	0.73	0.33	
0307 + 380	B	0.421 ± 0.007	$7.08^{+1.57}_{-0.99}$	132.310	+	−16.94	+0.01	0.816			+
	C	0.178 ± 0.003	$5.85^{+1.54}_{-0.91}$	33.472	+						
	D	0.347 ± 0.009	$13.02^{+2.04}_{-1.63}$	222.547	+						
	E	0.541 ± 0.005	$3.56^{+0.95}_{-0.57}$	6.742	+						
0322 + 222	D	0.855 ± 0.003	$1.51^{+0.37}_{-0.22}$	5.238	+	−28.02	−0.09	2.060		0.61	+
0323 + 342	C	0.339 ± 0.001	$1.05^{+0.54}_{-0.36}$	2.188		−18.76	−0.22	0.061			+
	D	0.351 ± 0.001	$0.57^{+0.28}_{-0.23}$	1.452							
0333 + 321	C	2.048 ± 0.005	$0.00^{+0.34}_{-0.34}$	0.361		−18.77	−0.10	1.258	0.88	0.36	+
	D	2.036 ± 0.003	$0.41^{+0.23}_{-0.20}$	1.178							
	E	1.977 ± 0.007	$0.00^{+0.71}_{-0.71}$	0.906							
0340 + 362	D	0.514 ± 0.007	$6.42^{+1.12}_{-0.78}$	66.610	+	−14.69	−0.14	1.484			+
0428 + 205	B	2.334 ± 0.004	$0.00^{+0.18}_{-0.18}$	0.110		−18.56	−0.39	0.219	3.22	0.06	
0430 + 289	E	0.230 ± 0.002	$3.69^{+1.03}_{-0.58}$	7.324	+	−12.60	−0.24	0.970			+
0507 + 179	B	0.642 ± 0.001	$0.17^{+0.25}_{-0.17}$	1.090		−12.79	+0.06	0.416	0.66	0.54	+
0529 + 483	B	0.564 ± 0.001	$0.00^{+0.26}_{-0.26}$	0.826		8.23	−0.03	1.162	0.47	0.67	+
	E	1.163 ± 0.006	$1.84^{+0.57}_{-0.34}$	2.855	+						
0602 + 405	B	1.042 ± 0.002	$0.00^{+0.36}_{-0.36}$	1.210		9.35	−0.17				
0633 + 734	B	0.834 ± 0.001	$0.00^{+0.14}_{-0.14}$	0.367		25.06	−0.08	1.850			+
0642 + 449	B	2.510 ± 0.004	$0.00^{+0.17}_{-0.17}$	0.159		17.95	−0.21	3.396	0.67	0.64	
0716 + 714	A	1.271 ± 0.005	$2.00^{+0.37}_{-0.25}$	4.345	+	28.02	+0.22	0.300	0.55	0.69	+
	B	1.629 ± 0.007	$2.21^{+0.35}_{-0.24}$	14.321	+						
	C	1.668 ± 0.008	$2.79^{+0.39}_{-0.28}$	9.358	+						
	D	1.301 ± 0.006	$2.97^{+0.39}_{-0.29}$	17.003	+						
	E	1.356 ± 0.005	$1.92^{+0.40}_{-0.29}$	2.805	+						
0730 + 504	D	0.436 ± 0.001	$0.54^{+0.25}_{-0.22}$	1.382		27.11	−0.09	0.720	0.38	0.45	+
0742 + 103	E	2.817 ± 0.011	$0.00^{+0.50}_{-0.50}$	0.341		16.59	−0.38	2.624	0.99	0.35	
0749 + 540	B	0.572 ± 0.002	$1.47^{+0.30}_{-0.20}$	6.029	+	30.51	−0.06	0.200	1.03	0.47	+
	C	0.634 ± 0.003	$2.15^{+0.41}_{-0.27}$	5.651	+						
	D	0.653 ± 0.002	$1.46^{+0.25}_{-0.17}$	4.565	+						
0804 + 499	A	0.672 ± 0.002	$0.00^{+0.34}_{-0.34}$	0.397		32.56	+0.05	1.435	0.34	0.78	+
	B	0.683 ± 0.001	$0.00^{+0.24}_{-0.24}$	0.641							
0812 + 367	C	0.963 ± 0.003	$0.17^{+0.52}_{-0.17}$	1.167		31.86	−0.17	1.027	0.76	0.67	
0814 + 425	A	1.018 ± 0.003	$0.60^{+0.40}_{-0.30}$	0.932		33.40	−0.27	0.530	0.94	0.48	+
	B	1.064 ± 0.002	$0.44^{+0.27}_{-0.22}$	1.531							
	E	1.029 ± 0.007	$5.07^{+0.53}_{-0.42}$	15.203	+						
0827 + 243	E	0.839 ± 0.004	$0.00^{+0.57}_{-0.57}$	0.524		31.88	+0.19	0.941			+

Table A1. *Cont.*

Name	Epoch	Flux Density [Jy]	$\overline{m}$ [%]	χ_r^2	IDV	b [°]	α	z	θ_5 [mas]	f_c	γ-ray
0831 + 557	A	5.344 ± 0.009	$0.00^{+0.28}_{-0.28}$	0.408		36.56	−0.66	0.241	3.10	0.04	
	B	5.372 ± 0.007	$0.00^{+0.14}_{-0.14}$	0.181							
	C	5.386 ± 0.010	$0.00^{+0.20}_{-0.20}$	0.097							
	D	5.393 ± 0.006	$0.00^{+0.12}_{-0.12}$	0.151							
0846 + 513	C	0.232 ± 0.001	$0.00^{+0.37}_{-0.37}$	0.658		39.14	+0.12	0.585	0.46	0.76	+
0851 + 202	D	3.119 ± 0.014	$1.77^{+0.44}_{-0.26}$	6.754	+	35.82	+0.13	0.306	0.50	0.46	+
	E	4.301 ± 0.017	$0.00^{+0.57}_{-0.57}$	0.456							
0859 + 470	A	1.432 ± 0.003	$0.00^{+0.26}_{-0.26}$	0.065		41.56	−0.36	1.465		0.64	+
	B	1.418 ± 0.002	$0.00^{+0.17}_{-0.17}$	0.300							
0917 + 449	A	1.053 ± 0.002	$0.00^{+0.34}_{-0.34}$	0.233		44.82	−0.13	2.186	0.54	0.72	+
0917 + 624	A	1.111 ± 0.002	$0.00^{+0.20}_{-0.20}$	0.256		40.99	−0.20	1.446	0.50	0.70	+
0923 + 392	A	10.324 ± 0.029	$0.00^{+0.36}_{-0.36}$	0.176		46.16	−0.20	0.695	0.70	0.62	
0925 + 504	A	0.336 ± 0.004	$3.87^{+1.11}_{-0.60}$	9.431	+	45.42	−0.01	0.370	0.57	0.70	+
	B	0.334 ± 0.002	$2.99^{+0.63}_{-0.38}$	18.678	+						
	C	0.447 ± 0.007	$7.17^{+1.36}_{-0.92}$	56.887	+						
	D	0.602 ± 0.006	$5.79^{+0.83}_{-0.61}$	60.041	+						
	E	0.350 ± 0.003	$4.54^{+0.78}_{-0.55}$	9.787	+						
0942 + 468	C	0.342 ± 0.001	$0.00^{+0.30}_{-0.30}$	0.247		48.83	−0.13	0.639	1.28	0.35	
0945 + 408	A	1.272 ± 0.003	$0.00^{+0.32}_{-0.32}$	0.161		50.28	−0.11	1.250	0.49	0.66	+
0951 + 693	C	0.220 ± 0.000	$0.00^{+0.36}_{-0.36}$	0.880		40.90	−0.11				
0954 + 658	A	1.567 ± 0.003	$0.00^{+0.25}_{-0.25}$	0.543		43.13	−0.04	0.368		0.89	+
	E	0.949 ± 0.002	$0.00^{+0.32}_{-0.32}$	0.510							
0955 + 326	A	0.951 ± 0.002	$0.00^{+0.30}_{-0.30}$	0.095		52.32	−0.33	0.531	0.64	0.37	
0955 + 476	A	0.914 ± 0.002	$0.26^{+0.32}_{-0.26}$	0.777		50.73	−0.06	1.882	0.31	0.87	+
1015 + 359	A	0.553 ± 0.002	$0.64^{+0.41}_{-0.30}$	0.679		56.43	+0.09	1.230	0.35	0.64	+
1040 + 244	E	0.784 ± 0.006	$2.39^{+0.81}_{-0.44}$	3.876	+	61.01	+0.02	0.563	0.39	0.69	+
1044 + 476	C	0.405 ± 0.001	$0.00^{+0.33}_{-0.33}$	0.275		58.44	−0.43	0.799	1.77	0.47	
1044 + 719	A	2.320 ± 0.003	$0.00^{+0.24}_{-0.24}$	0.505		42.29	−0.16	1.150	0.37	0.70	+
	E	3.349 ± 0.007	$0.00^{+0.34}_{-0.34}$	0.574							
1053 + 815	A	0.381 ± 0.001	$0.99^{+0.26}_{-0.19}$	1.122		34.75	−0.01	0.706			+
1101 + 384	A	0.634 ± 0.002	$0.00^{+0.40}_{-0.40}$	0.634		65.03	−0.10	0.030		0.85	+
	E	0.617 ± 0.002	$0.00^{+0.56}_{-0.56}$	0.569							
1123 + 264	A	1.248 ± 0.003	$0.00^{+0.30}_{-0.30}$	0.212		70.89	−0.03	2.352	0.34	0.71	
	B	1.250 ± 0.002	$0.00^{+0.33}_{-0.33}$	0.829							
	C	1.227 ± 0.003	$0.00^{+0.37}_{-0.37}$	0.390							
	D	1.253 ± 0.003	$0.56^{+0.30}_{-0.22}$	1.491							
	E	1.225 ± 0.005	$0.00^{+0.46}_{-0.46}$	0.185							
1125 + 596	A	0.692 ± 0.004	$3.28^{+0.55}_{-0.37}$	9.795	+	54.67	−0.02	1.795	0.24	0.78	+
	C	0.773 ± 0.006	$4.29^{+0.61}_{-0.44}$	20.143	+						
	D	0.807 ± 0.008	$6.28^{+0.76}_{-0.60}$	76.008	+						
	E	0.840 ± 0.005	$3.66^{+0.58}_{-0.41}$	8.054	+						
1144 + 402	A	1.797 ± 0.004	$0.00^{+0.45}_{-0.45}$	0.489		71.47	−0.00	1.090	0.23	0.73	+
	D	1.327 ± 0.002	$0.00^{+0.28}_{-0.28}$	0.703							
1150 + 497	D	1.377 ± 0.002	$0.00^{+0.20}_{-0.20}$	0.462		64.98	−0.10	0.334	0.73	0.50	+
1150 + 812	B	1.172 ± 0.001	$0.00^{+0.12}_{-0.12}$	0.178		35.84	−0.05	1.250		0.51	
1156 + 295	A	1.167 ± 0.003	$0.00^{+0.29}_{-0.29}$	0.140		78.37	−0.17	0.725	0.61	0.77	+
	B	1.153 ± 0.004	$1.24^{+0.37}_{-0.22}$	5.142	+						
	C	1.442 ± 0.005	$0.66^{+0.50}_{-0.38}$	1.548							
	D	1.521 ± 0.003	$0.72^{+0.28}_{-0.18}$	1.906							
	E	1.645 ± 0.005	$0.00^{+0.71}_{-0.71}$	0.967							
1214 + 588	B	0.732 ± 0.001	$0.00^{+0.14}_{-0.14}$	0.348		57.97	−0.13	2.551	0.89	0.36	
	C	0.763 ± 0.001	$0.00^{+0.21}_{-0.21}$	0.289							
1219 + 285	D	0.722 ± 0.001	$0.00^{+0.31}_{-0.31}$	0.695		83.29	−0.09	0.102	0.58	0.36	+
1222 + 216	E	2.541 ± 0.010	$0.00^{+0.46}_{-0.46}$	0.056		81.66	−0.27	0.432		0.78	+
1333 + 589	B	0.701 ± 0.002	$1.05^{+0.22}_{-0.15}$	3.800	+	57.48	+0.16	0.570	1.44	0.20	
	C	0.704 ± 0.001	$0.70^{+0.30}_{-0.24}$	1.528							
1357 + 769	A	0.392 ± 0.001	$1.32^{+0.34}_{-0.22}$	1.741		39.77	−0.10	1.585	0.42	0.82	+
	E	0.196 ± 0.001	$4.28^{+0.48}_{-0.39}$	8.218	+						
1404 + 286	D	2.154 ± 0.004	$0.00^{+0.19}_{-0.19}$	0.200		73.25	+0.00			0.94	0.40

Table A1. *Cont.*

Name	Epoch	Flux Density [Jy]	$\overline{m}$ [%]	χ_r^2	IDV	b [°]	α	z	θ_5 [mas]	f_c	γ-ray
1417 + 385	C	0.618 ± 0.003	$1.19^{+0.52}_{-0.30}$	2.528	+	68.38	+0.02	1.830	0.48	0.86	+
	D	0.543 ± 0.002	$1.02^{+0.32}_{-0.22}$	2.597	+						
1435 + 638	A	1.493 ± 0.002	$0.00^{+0.19}_{-0.19}$	0.106		49.73	−0.36	2.068	1.11	0.33	
1520 + 319	B	0.471 ± 0.001	$0.00^{+0.41}_{-0.41}$	1.121		57.02	−0.01	1.487	0.32	0.84	+
1547 + 507	C	0.782 ± 0.006	$3.93^{+0.66}_{-0.46}$	15.284	+	49.06	−0.02	2.171	1.03	0.56	
	D	0.792 ± 0.005	$3.29^{+0.57}_{-0.38}$	18.832	+						
	E	0.806 ± 0.007	$4.06^{+0.87}_{-0.56}$	7.844	+						
1617 + 229	D	0.652 ± 0.003	$1.75^{+0.49}_{-0.28}$	6.534	+	43.03	−0.05	1.987	0.29	0.84	
1633 + 382	A	2.683 ± 0.006	$0.00^{+0.30}_{-0.30}$	0.280		42.34	−0.14	1.813	1.14	0.18	+
	B	2.727 ± 0.004	$0.00^{+0.19}_{-0.19}$	0.268							
	C	2.365 ± 0.006	$0.00^{+0.42}_{-0.42}$	0.696							
	E	2.207 ± 0.005	$0.00^{+0.24}_{-0.24}$	0.148							
1638 + 398	C	1.328 ± 0.003	$0.00^{+0.31}_{-0.31}$	0.270		41.42	−0.08	1.660	0.28	0.82	+
1641 + 399	A	5.975 ± 0.012	$0.00^{+0.24}_{-0.24}$	0.157		40.95	−0.20	0.593	1.28	0.24	+
1642 + 264	D	0.084 ± 0.000	$0.70^{+0.57}_{-0.66}$	1.286		38.40	−0.21				
1642 + 690	E	1.860 ± 0.005	$0.00^{+0.30}_{-0.30}$	0.171		36.62	−0.12	0.751	0.75	0.50	
1714 + 219	E	0.534 ± 0.003	$0.00^{+0.60}_{-0.60}$	0.139		30.22	−0.17	0.358			
1726 + 455	C	1.217 ± 0.004	$0.44^{+0.37}_{-0.34}$	1.275		33.28	+0.00	0.717	0.34	0.87	+
	D	1.559 ± 0.003	$0.00^{+0.29}_{-0.29}$	0.646							
1751 + 288	B	1.684 ± 0.002	$0.00^{+0.16}_{-0.16}$	0.123		24.46	+0.08	1.115	0.82	0.86	
	C	1.731 ± 0.005	$0.00^{+0.43}_{-0.43}$	0.627							
1758 + 388	B	0.738 ± 0.001	$0.00^{+0.26}_{-0.26}$	0.817		26.03	−0.16	2.092	0.30	0.87	
	C	0.697 ± 0.002	$0.00^{+0.39}_{-0.39}$	0.550							
1807 + 279	B	0.653 ± 0.001	$0.00^{+0.17}_{-0.17}$	0.198		20.97	−0.39	1.760			
	D	0.624 ± 0.002	$0.72^{+0.32}_{-0.19}$	1.843							
1807 + 698	A	1.799 ± 0.003	$0.00^{+0.27}_{-0.27}$	0.425		29.17	−0.08	0.051	0.83	0.64	+
	B	1.803 ± 0.002	$0.00^{+0.14}_{-0.14}$	0.493							
1817 + 387	C	0.159 ± 0.001	$1.69^{+0.56}_{-0.32}$	3.412	+	22.46	+0.56	0.540			
	E	0.219 ± 0.001	$0.00^{+0.62}_{-0.62}$	0.530							
1823 + 568	B	1.128 ± 0.002	$0.99^{+0.22}_{-0.14}$	3.527	+	26.08	−0.03	0.664	0.43	0.82	+
1842 + 681	C	0.662 ± 0.001	$0.54^{+0.27}_{-0.27}$	1.322		25.85	−0.09	0.472		0.77	+
1843 + 356	C	0.784 ± 0.002	$0.00^{+0.34}_{-0.34}$	0.348		16.53	−0.22	0.764			
1846 + 322	C	0.572 ± 0.003	$1.29^{+0.52}_{-0.31}$	2.781	+	14.71	−0.12	0.798	4.49		+
	D	0.506 ± 0.002	$1.06^{+0.33}_{-0.21}$	2.796	+						
1849 + 670	A	1.226 ± 0.003	$0.95^{+0.27}_{-0.20}$	1.209		25.04	+0.19	0.657	0.54	0.86	+
	B	1.257 ± 0.002	$0.84^{+0.20}_{-0.13}$	2.991	+						
1850 + 402	E	0.713 ± 0.003	$0.00^{+0.42}_{-0.42}$	0.113		16.97	−0.07	2.120			
1923 + 210	C	1.406 ± 0.004	$0.00^{+0.33}_{-0.33}$	0.256		2.26	−0.12		1.29	0.21	
1926 + 611	A	0.960 ± 0.007	$3.57^{+0.64}_{-0.42}$	11.904	+	19.45	−0.04		0.71	0.64	+
	E	0.916 ± 0.002	$0.00^{+0.43}_{-0.43}$	0.722							
1928 + 738	B	3.032 ± 0.003	$0.00^{+0.16}_{-0.16}$	0.567		23.54	−0.24	0.302	1.01	0.50	
1954 + 513	C	1.469 ± 0.003	$0.00^{+0.33}_{-0.33}$	0.771		11.76	−0.22	1.220	0.66	0.67	
	E	1.370 ± 0.004	$0.00^{+0.55}_{-0.55}$	0.771							
2005 + 403	C	2.331 ± 0.006	$0.00^{+0.34}_{-0.34}$	0.389		4.30	−0.12	1.736			
2005 + 642	A	0.487 ± 0.001	$0.00^{+0.41}_{-0.41}$	0.553		16.73	+0.38	1.574			
2007 + 777	B	0.700 ± 0.002	$1.27^{+0.24}_{-0.16}$	5.390	+	22.73	−0.19	0.342	0.72	0.64	+
	D	0.761 ± 0.003	$2.35^{+0.32}_{-0.23}$	10.748	+						
2010 + 723	A	0.878 ± 0.002	$1.10^{+0.30}_{-0.21}$	1.923		20.18	−0.27				
2013 + 370	E	3.890 ± 0.014	$0.00^{+0.43}_{-0.43}$	0.158		1.22	−0.03				+
2021 + 614	D	3.107 ± 0.003	$0.00^{+0.16}_{-0.16}$	0.559		13.78	−0.19	0.227	0.79	0.36	
2022 + 542	C	0.664 ± 0.001	$0.00^{+0.26}_{-0.26}$	0.570		9.66	−0.90			0.30	
2023 + 760	A	0.714 ± 0.003	$1.43^{+0.35}_{-0.22}$	2.677	+	21.13	+0.07	0.594			+
2107 + 353	C	1.093 ± 0.003	$0.00^{+0.51}_{-0.51}$	0.852		−8.35	+0.13	0.202	1.48	0.18	+
2136 + 141	E	2.438 ± 0.011	$0.00^{+0.52}_{-0.52}$	0.293		−27.54	−0.14	2.427	0.60	0.66	
2155 + 312	B	0.418 ± 0.001	$1.27^{+0.33}_{-0.20}$	4.932	+	−18.24	+0.02	1.486			+
	E	0.645 ± 0.004	$1.69^{+0.79}_{-0.42}$	2.416							
2200 + 420	D	3.060 ± 0.005	$0.56^{+0.24}_{-0.17}$	1.473		−10.44	−0.08	0.069	0.37	0.45	+
	E	2.146 ± 0.007	$0.00^{+0.62}_{-0.62}$	0.793							
2201 + 315	C	2.465 ± 0.006	$0.00^{+0.28}_{-0.28}$	0.148		−18.78	−0.09	0.295	0.94	0.45	+

Table A1. *Cont.*

Name	Epoch	Flux Density [Jy]	$\overline{m}$ [%]	χ_r^2	IDV	b [°]	α	z	θ_5 [mas]	f_c	γ-ray
2209 + 236	C	0.796 ± 0.003	$0.45^{+0.39}_{-0.37}$	1.310		-26.09	$+0.13$	1.125		0.85	+
	D	1.059 ± 0.003	$1.07^{+0.34}_{-0.20}$	3.085	+						
2223 + 210	C	1.547 ± 0.004	$0.00^{+0.35}_{-0.35}$	0.444		-30.09	-0.24	1.959	1.26	0.17	
	D	1.593 ± 0.003	$0.00^{+0.18}_{-0.18}$	0.143							
2230 + 114	E	4.235 ± 0.017	$0.00^{+0.46}_{-0.46}$	0.117		-38.58	-0.20	1.037	1.04	0.40	+
2309 + 454	B	0.699 ± 0.003	$1.69^{+0.37}_{-0.23}$	7.917	+	-13.70	$+0.13$	1.447			
	D	0.530 ± 0.003	$2.40^{+0.47}_{-0.30}$	10.230	+						
	E	0.550 ± 0.003	$1.28^{+0.61}_{-0.39}$	1.766							
2351 + 456	B	1.142 ± 0.002	$0.00^{+0.15}_{-0.15}$	0.152		-15.85	-0.26	1.992		0.50	+

References

1. Kovalev, Y.; Kardashev, N.S.; RadioAstron Collaboration. Space VLBI mission RadioAstron: Current status and early science program. In Proceedings of the Meeting "Resolving The Sky—Radio Interferometry: Past, Present and Future", Manchester, UK, 17–20 April 2012; p. 40.
2. Sokolovsky, K.V. RadioAstron Early Science Program Space-VLBI AGN survey: Strategy and first results. *arXiv* **2013**, arXiv:1303.5451.[CrossRef]
3. Kovalev, Y.Y.; Kardashev, N.S.; Kellermann, K.I.; Edwards, P.G. The RadioAstron space VLBI project. In Proceedings of the 2014 XXXIth URSI General Assembly and Scientific Symposium (URSI GASS), Beijing, China, 16–23 August 2014.
4. Witzel, A.; Heeschen, D.S.; Schalinski, C.; Krichbaum, T. Kurzzeit-Variabilität extragalaktischer Radioquellen. *Mitteilungen der Astronomischen Gesellschaft Hamburg* **1986**, *65*, 239.
5. Heeschen, D.S.; Krichbaum, T.; Schalinski, C.J.; Witzel, A. Rapid variability of extragalactic radio sources. *Astron. J.* **1987**, *94*, 1493–1507.[CrossRef]
6. Quirrenbach, A. Variability and VLBI Observations of Extragalactic Radio Surces. In *Reviews in Modern Astronomy*; Klare, G., Ed.; Springer: Berlin/Heidelberg, Germany, 1992; Volume 5, pp. 214–228.
7. Lovell, J.E.J.; Rickett, B.J.; Macquart, J.P.; Jauncey, D.L.; Bignall, H.E.; Kedziora-Chudczer, L.; Ojha, R.; Pursimo, T.; Dutka, M.; Senkbeil, C.; et al. The Micro-Arcsecond Scintillation-Induced Variability (MASIV) Survey. II. The First Four Epochs. *Astrophys. J.* **2008**, *689*, 108–126.[CrossRef]
8. Kedziora-Chudczer, L.; Jauncey, D.L.; Wieringa, M.H.; Walker, M.A.; Nicolson, G.D.; Reynolds, J.E.; Tzioumis, A.K. PKS 0405-385: The Smallest Radio Quasar? *Astrophys. J. Lett.* **1997**, *490*, L9–L12.[CrossRef]
9. Jauncey, D.L.; Macquart, J.P. Intra-day variability and the interstellar medium towards 0917 + 624. *Astron. Astrophys.* **2001**, *370*, L9–L12.[CrossRef]
10. Dennett-Thorpe, J.; de Bruyn, A.G. Interstellar scintillation as the origin of the rapid radio variability of the quasar J1819 + 3845. *Nature* **2002**, *415*, 57–60.[CrossRef]
11. Bignall, H.E.; Jauncey, D.L.; Lovell, J.E.J.; Tzioumis, A.K.; Kedziora-Chudczer, L.; Macquart, J.P.; Tingay, S.J.; Rayner, D.P.; Clay, R.W. Rapid Variability and Annual Cycles in the Characteristic Timescale of the Scintillating Source PKS 1257-326. *Astrophys. J.* **2003**, *585*, 653–664.[CrossRef]
12. Bignall, H.E.; Macquart, J.P.; Jauncey, D.L.; Lovell, J.E.J.; Tzioumis, A.K.; Kedziora-Chudczer, L. Rapid Interstellar Scintillation of PKS 1257-326: Two-Station Pattern Time Delays and Constraints on Scattering and Microarcsecond Source Structure. *Astrophys. J.* **2006**, *652*, 1050–1058.[CrossRef]
13. Liu, B.R.; Liu, X.; Marchili, N.; Liu, J.; Mi, L.G.; Krichbaum, T.P.; Fuhrmann, L.; Zensus, J.A. Two-year monitoring of intra-day variability of quasar 1156 + 295 at 4.8 GHz. *Astron. Astrophys.* **2013**, *555*, A134.[CrossRef]
14. Qian, S.J.; Zhang, X.Z. An Intrinsic Model for the Polarization Position Angle Swing Observed in QSO 1150 + 812. *J. Astron. Astrophys.* **2004**, *4*, 37–50.[CrossRef]
15. Krichbaum, T.P.; Witzel, A.; Zensus, J.A. The Role of Millimeter VLBI Observations in AGN Research. *arXiv* **2002**, arXiv:astro-ph/0204062.[CrossRef]
16. Wagner, S.J.; Witzel, A.; Heidt, J.; Krichbaum, T.P.; Qian, S.J.; Quirrenbach, A.; Wegner, R.; Aller, H.; Aller, M.; Anton, K.; et al. Rapid Variability in S5 0716 + 714 Across the Electromagnetic Spectrum. *Astron. J.* **1996**, *111*, 2187.[CrossRef]

17.   Liu, X.; Mi, L.G.; Liu, J.; Cui, L.; Song, H.G.; Krichbaum, T.P.; Kraus, A.; Fuhrmann, L.; Marchili, N.; Zensus, J.A. Intra-day variability observations and the VLBI structure analysis of quasar S4 0917 + 624. *Astron. Astrophys.* **2015**, *578*, A34.[CrossRef]

18.   Kellermann, K.I.; Pauliny-Toth, I.I.K. The Spectra of Opaque Radio Sources. *Astrophys. J. Lett.* **1969**, *155*, L71.[CrossRef]

19.   Kovalev, Y.Y.; Kardashev, N.S.; Kellermann, K.I.; Lobanov, A.P.; Johnson, M.D.; Gurvits, L.I.; Voitsik, P.A.; Zensus, J.A.; Anderson, J.M.; Bach, U.; et al. RadioAstron Observations of the Quasar 3C273: A Challenge to the Brightness Temperature Limit. *Astrophys. J. Lett.* **2016**, *820*, L9.[CrossRef]

20.   Johnson, M.D.; Kovalev, Y.Y.; Gwinn, C.R.; Gurvits, L.I.; Narayan, R.; Macquart, J.P.; Jauncey, D.L.; Voitsik, P.A.; Anderson, J.M.; Sokolovsky, K.V.; et al. Extreme Brightness Temperatures and Refractive Substructure in 3C273 with RadioAstron. *Astrophys. J. Lett.* **2016**, *820*, L10.[CrossRef]

21.   Liu, J.; Liu, X.; Cui, L.; Ding, Z.; Krichbaum, T.P.; Kraus, A.; Marchili, N.; Zensus, J.A. UNSS: The Urumqi Northern Sky Survey for Rapid Variability in Compact Radio Sources. in press.

22.   Lovell, J.E.J.; Jauncey, D.L.; Bignall, H.E.; Kedziora-Chudczer, L.; Macquart, J.P.; Rickett, B.J.; Tzioumis, A.K. First Results from MASIV: The Microarcsecond Scintillation-induced Variability Survey. *Astron. J.* **2003**, *126*, 1699–1706.[CrossRef]

23.   Kraus, A.; Krichbaum, T.P.; Wegner, R.; Witzel, A.; Cimò, G.; Quirrenbach, A.; Britzen, S.; Fuhrmann, L.; Lobanov, A.P.; Naundorf, C.E.; et al. Intraday variability in compact extragalactic radio sources. II. Observations with the Effelsberg 100 m radio telescope. *Astron. Astrophys.* **2003**, *401*, 161–172.

24.   Baars, J.W.M.; Genzel, R.; Pauliny-Toth, I.I.K.; Witzel, A. The absolute spectrum of CAS A—An accurate flux density scale and a set of secondary calibrators. *Astron. Astrophys.* **1977**, *61*, 99–106.

25.   Ott, M.; Witzel, A.; Quirrenbach, A.; Krichbaum, T.P.; Standke, K.J.; Schalinski, C.J.; Hummel, C.A. An updated list of radio flux density calibrators. *Astron. Astrophys.* **1994**, *284*, 331–339.

26.   Fuhrmann, L.; Krichbaum, T.P.; Witzel, A.; Kraus, A.; Britzen, S.; Bernhart, S.; Impellizzeri, C.M.V.; Agudo, I.; Klare, J.; Sohn, B.W.; et al. Testing the inverse-Compton catastrophe scenario in the intra-day variable blazar S5 0716 + 71. III. Rapid and correlated flux density variability from radio to sub-mm bands. *Astron. Astrophys.* **2008**, *490*, 1019–1037.[CrossRef]

27.   Richards, J.L.; Max-Moerbeck, W.; Pavlidou, V.; King, O.G.; Pearson, T.J.; Readhead, A.C.S.; Reeves, R.; Shepherd, M.C.; Stevenson, M.A.; Weintraub, L.C.; et al. Blazars in the Fermi Era: The OVRO 40 m Telescope Monitoring Program. *Astrophys. J. Suppl. Ser.* **2011**, *194*, 29.[CrossRef]

28.   Acero, F.; Ackermann, M.; Ajello, M.; Albert, A.; Atwood, W.B.; Axelsson, M.; Baldini, L.; Ballet, J.; Barbiellini, G.; Bastieri, D.; et al. Fermi Large Area Telescope Third Source Catalog. *Astrophys. J. Suppl. Ser.* **2015**, *218*, 23.[CrossRef]

29.   Pushkarev, A.B.; Kovalev, Y.Y. Milky Way scattering properties and intrinsic sizes of active galactic nuclei cores probed by very long baseline interferometry surveys of compact extragalactic radio sources. *Mon. Not. R. Astron. Soc.* **2015**, *452*, 4274–4282.[CrossRef]

30.   Richards, J.L.; Hovatta, T.; Max-Moerbeck, W.; Pavlidou, V.; Pearson, T.J.; Readhead, A.C.S. Connecting radio variability to the characteristics of gamma-ray blazars. *Mon. Not. R. Astron. Soc.* **2014**, *438*, 3058–3069.[CrossRef]

31.   Scholz, F.W.; Stephens, M.A. K-sample Anderson–Darling Tests. *J. Am. Stat. Assoc.* **1974**, *82*, 918–924.

32.   Bignall, H.E.; Jauncey, D.L.; Lovell, J.E.J.; Kedziora-Chudczer, L.; Macquart, J.P.; Tzioumis, A.K.; Rickett, B.J.; Ojha, R.; Carter, S.; Cimó, G.; et al. Interstellar scintillation as a probe of microarcsecond scale structure in quasars. In Proceedings of the European VLBI Network on New Developments in VLBI Science and Technology, Toledo, Spain, 12–15 October 2004; pp. 19–22.

33.   Dennett-Thorpe, J.; de Bruyn, A.G. The Discovery of a Microarcsecond Quasar: J1819 + 3845. *Astrophys. J. Lett.* **2000**, *529*, L65–L68.[CrossRef]

34.   Readhead, A.C.S. Equipartition brightness temperature and the inverse Compton catastrophe. *Astrophys. J.* **1994**, *426*, 51–59.[CrossRef]

35.   Heeschen, D.S. Flickering of extragalactic radio sources. *Astron. J.* **1984**, *89*, 1111–1123.[CrossRef]

36.   Kovalev, Y.Y.; Aller, H.D.; Aller, M.F.; Homan, D.C.; Kadler, M.; Kellermann, K.I.; Kovalev, Y.A.; Lister, M.L.; McCormick, M.J.; Pushkarev, A.B.; et al. The Relation Between AGN Gamma-Ray Emission and Parsec-Scale Radio Jets. *Astrophys. J. Lett.* **2009**, *696*, L17–L21.[CrossRef]

37. Pushkarev, A.B.; Kovalev, Y.Y.; Lister, M.L. Radio/Gamma-ray Time Delay in the Parsec-scale Cores of Active Galactic Nuclei. *Astrophys. J. Lett.* **2010**, *722*, L7–L11.[CrossRef]

38. Lister, M.L.; Homan, D.C.; Kadler, M.; Kellermann, K.I.; Kovalev, Y.Y.; Ros, E.; Savolainen, T.; Zensus, J.A. A Connection Between Apparent VLBA Jet Speeds and Initial Active Galactic Nucleus Detections Made by the Fermi Gamma-Ray Observatory. *Astrophys. J. Lett.* **2009**, *696*, L22–L26.[CrossRef]

39. Ramakrishnan, V.; León-Tavares, J.; Rastorgueva-Foi, E.A.; Wiik, K.; Jorstad, S.G.; Marscher, A.P.; Tornikoski, M.; Agudo, I.; Lähteenmäki, A.; Valtaoja, E.; et al. The connection between the parsec-scale radio jet and γ-ray flares in the blazar 1156 + 295. *Mon. Not. R. Astron. Soc.* **2014**, *445*, 1636–1646.[CrossRef]

40. Casadio, C.; Gómez, J.L.; Grandi, P.; Jorstad, S.G.; Marscher, A.P.; Lister, M.L.; Kovalev, Y.Y.; Savolainen, T.; Pushkarev, A.B. The Connection between the Radio Jet and the Gamma-ray Emission in the Radio Galaxy 3C 120. *Astrophys. J.* **2015**, *808*, 162.[CrossRef]

41. Hada, K.; Kino, M.; Doi, A.; Nagai, H.; Honma, M.; Akiyama, K.; Tazaki, F.; Lico, R.; Giroletti, M.; Giovannini, G.; et al. High-sensitivity 86 GHz (3.5 mm) VLBI Observations of M87: Deep Imaging of the Jet Base at a Resolution of 10 Schwarzschild Radii. *Astrophys. J.* **2016**, *817*, 131.[CrossRef]

42. Haffner, L.M.; Reynolds, R.J.; Tufte, S.L.; Madsen, G.J.; Jaehnig, K.P.; Percival, J.W. The Wisconsin Hα Mapper Northern Sky Survey. *Astrophys. J. Suppl. Ser.* **2003**, *149*, 405–422.[CrossRef]

43. Rickett, B.J.; Lazio, T.J.W.; Ghigo, F.D. Interstellar Scintillation Observations of 146 Extragalactic Radio Sources. *Astrophys. J. Suppl. Ser.* **2006**, *165*, 439–460.[CrossRef]

44. Lazio, J.; Ojha, R.; Fey, A.L.; Kedziora-Chudczer, L.; Cordes, J.M.; Jauncey, D.L.; Lovell, J.E. Milliarcsecond Observations of Microarcsecond AGN. In Proceedings of the Conference "Frontiers of Astrophysics: A Celebration of NRAO's 50th Anniversary", Charlottesville, VA, USA, 18–21 June 2007; p. 372.

45. Ojha, R.; Fey, A.L.; Jauncey, D.L.; Lovell, J.E.J.; Johnston, K.J. Milliarcsecond Structure of Microarcsecond Sources: Comparison of Scintillating and Nonscintillating Extragalactic Radio Sources. *Astrophys. J.* **2004**, *614*, 607–614.[CrossRef]

46. Hovatta, T.; Valtaoja, E.; Tornikoski, M.; Lähteenmäki, A. Doppler factors, Lorentz factors and viewing angles for quasars, BL Lacertae objects and radio galaxies. *Astron. Astrophys.* **2009**, *494*, 527–537.[CrossRef]

47. Savolainen, T.; Homan, D.C.; Hovatta, T.; Kadler, M.; Kovalev, Y.Y.; Lister, M.L.; Ros, E.; Zensus, J.A. Relativistic beaming and gamma-ray brightness of blazars. *Astron. Astrophys.* **2010**, *512*, A24.[CrossRef]

48. Maraschi, L.; Ghisellini, G.; Celotti, A. A jet model for the gamma-ray emitting blazar 3C 279. *Astrophys. J. Lett.* **1992**, *397*, L5–L9.[CrossRef]

49. Dermer, C.D.; Schlickeiser, R.; Mastichiadis, A. High-energy gamma radiation from extragalactic radio sources. *Astron. Astrophys.* **1992**, *256*, L27–L30.

50. Sikora, M.; Begelman, M.C.; Rees, M.J. Comptonization of diffuse ambient radiation by a relativistic jet: The source of gamma rays from blazars? *Astrophys. J.* **1994**, *421*, 153–162.[CrossRef]

51. Mannheim, K. The proton blazar. *Astron. Astrophys.* **1993**, *269*, 67–76.

52. Marscher, A.P. Accurate formula for the self-Compton X-ray flux density from a uniform, spherical, compact radio source. *Astrophys. J.* **1983**, *264*, 296.[CrossRef]

53. Lee, S.S.; Lobanov, A.P.; Krichbaum, T.P.; Zensus, J.A. Acceleration of Compact Radio Jets on Sub-parsec Scales. *Astrophys. J.* **2016**, *826*, 135.[CrossRef]

54. Hollenbach, D.J.; Tielens, A.G.G.M. Dense Photodissociation Regions (PDRs). *Annu. Rev. Astron. Astrophys.* **1997**, *35*, 179–216.[CrossRef]

55. Magnani, L.; Hartmann, D.; Speck, B.G. A Catalog of Molecular Gas at High Galactic Latitudes. *Astrophys. J. Suppl. Ser.* **1996**, *106*, 447.[CrossRef]

56. Redfield, S.; Linsky, J.L. The Structure of the Local Interstellar Medium. IV. Dynamics, Morphology, Physical Properties, and Implications of Cloud-Cloud Interactions. *Astrophys. J.* **2008**, *673*, 283–314.[CrossRef]

57. Walker, M.A.; Tuntsov, A.V.; Bignall, H.; Reynolds, C.; Bannister, K.W.; Johnston, S.; Stevens, J.; Ravi, V. Extreme Radio-wave Scattering Associated with Hot Stars. *Astrophys. J.* **2017**, *843*, 15.

58. Pearson, T.J. Non-Imaging Data Analysis. In *Synthesis Imaging in Radio Astronomy II*; Taylor, G.B., Carilli, C.L., Perley, R.A., Eds.; Astronomical Society of the Pacific: San Francisco, CA, USA, 1999; Volume 180, p. 335.